Membrane heterogeneity : from lipid domains to curvature effects

Semrau, S.

Chapter 1

Introduction[1]

The length scales studied in experiments today comprise many orders of magnitude: from subatomic structure unraveled by large particle accelerators to galaxies many lightyears away imaged by space born telescopes. Despite the technical sophistication, which makes this wide range accessible, there are still systems that defy the resolution of their organization on a micrometer to nanometer scale. One of them is the cell membrane. The sheer complexity of this nanometer-thin fluid material has been challenging biologists and physicist for many years. One of the first models that captured essential features of the cell membrane is the homogeneous fluid mosaic model (1). This model was refined by including heterogeneity (Fig. 1.1), where either the lipid composition or the proteins were given the leading role. Both concepts are in the process of being reconciled in the light of new experiments on lipid-protein interactions. Those interactions range from specific chemical to unspecific and purely physical. The latter comprise membrane curvature mediated interactions which have recently been shown to influence a large number of biological processes. In parallel to the conception of refined models, new experimental techniques to determine membrane microstructure were developed. Single molecule fluorescence has emerged as one of the leading technologies since it delivers the required spatial resolution and can be employed in living cells. In a

[1] This chapter is based on: S. Semrau, T. Schmidt Membrane heterogeneity - From lipid domains to curvature effects, *Soft Matter*, **5** (17), 3174-3186 (2009)

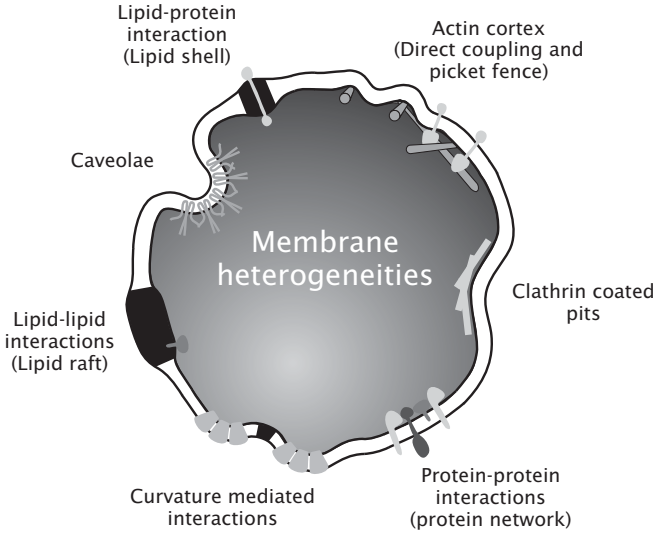

Figure 1.1
Membrane heterogeneities

complementary approach artificial model systems are used to study specific biophysical aspects of membranes in isolation and in a controllable way. Nowadays, artificial membranes have outgrown their initial status as simplistic mock cells: a rich spectrum of different phases and phase transitions and the unique possibility to study membrane material properties make them an exciting subject of research in their own right (2, 3). In this thesis we show how phase separated artificial membranes can be used to gain fundamental insight into lipid composition based heterogeneity (Chap. 2) and membrane mediated interactions (Chap. 3). We demonstrate that those interactions can lead to lipid domain sorting (Chap. 4). Experiments with artificial membranes are complemented with live cell studies. We develop a robust analysis method for single molecule position (Chap. 5) and use it to study the role of heterogeneity in cell signaling (Chap. 6). Finally, we show how protein cluster formation can be measured by counting single molecules in live cells (Chap. 7).

1.1 Membrane heterogeneity

The plasma membrane is a complex, self assembled composite material fulfilling a host of different functions. Historically, the membrane was mainly considered a semi-permeable barrier necessary for maintaining biochemical conditions that are different from the environment. Homeostasis and metabolism require highly selective permeability for certain molecules, which is provided by ion channels and active transporters. While membrane asymmetry - a difference in composition between the two leaflets of the lipid bilayer - might influence membrane permeability, the barrier function of the membrane does not imply any lateral structure. Correspondingly, early models of the membrane sketched it as a homogeneous, liquid mosaic (1). As more and more elaborate functions of the cell membrane were identified, this image of the membrane structure had to be refined (4). Being much more than a simple barrier, the membrane serves as a two-dimensional reaction platform for a plethora of biochemical reactions. For these reactions to take place quickly and efficiently, the membrane was suggested to be compartmentalized (5–7). In this way the composition of local environments could be optimized for the functioning of certain membrane proteins. (8, 9). For example, some G protein coupled receptors translocate after ligand binding to specific microdomains, where they interact with their G protein (10, 11) (Chap. 6 of this thesis). Confinement to small domains diminishes the time for a receptor and cofactors to meet and therefore speeds up signaling (12). Microdomains also serve as platforms for receptor internalization and therefore desensitization (13). Furthermore, they are speculated to serve as entry ports for viruses (14) and to play a vital role in immunology (15). While many biological functions have been shown to depend on local environments with specific compositions, the physical nature and the driving forces for their formation are still discussed and many different kinds of microdomains have been identified, see Fig. 1.1.

The "lipid raft" model champions lipid composition as the major driving force for heterogeneity (8, 9). A lipid raft was thought to be a membrane domain which is enriched in sphingolipids and cholesterol (liquid ordered phase), see Fig. 1.2. Artificial membranes made from (unsaturated) phospholipids, (fully saturated) sphingolipids and cholesterol spontaneously phase separate into a (liquid ordered) "raft" phase and a liquid disordered phase. These phases, which differ in their lipid tail organization, have the ability to differentially segregate proteins *in vitro* (16, 17).

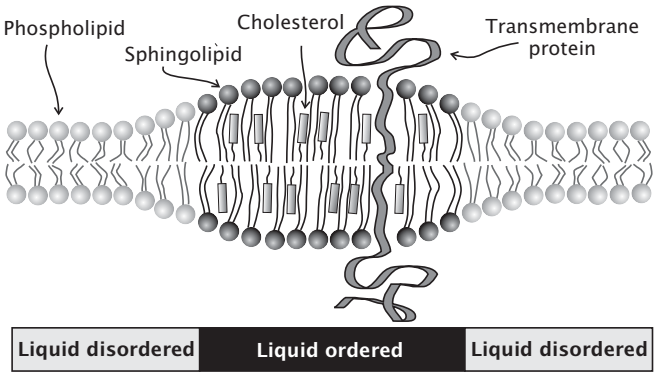

Figure 1.2
Liquid ordered and liquid disordered phase differ in composition, lipid tail order and thickness

Biochemical assays on cells, based on detergent resistance and cholesterol depletion, seemed to suggest that certain proteins can be found in such domains *in vivo* too. The significance of those experiments is, however, questionable (18): detergent and cholesterol depletion are suspected to induce the formation of domains. Additionally, lipid rafts were found to be at most a few tens of *nm* in diameter, which means they could transport only a few proteins (19, 20) (Chap. 2 of this thesis). Furthermore, the binary picture of the cell membrane divided in raft and non-raft regions is oversimplified: Not only that the membrane contains significantly more than 3 different types of lipids which could result in several liquid phases all with different properties. Even with only 3 components, membranes that are asymmetric - the compositions of the two leaflets are different - exhibit 3 distinguishable phases (21). Also the idea that rafts are stable entities was challenged (19). Recent experiments (22, 23) suggest that the membrane of a live cell at physiological temperatures is close to a miscibility critical point which implies strong composition fluctuations. The question is then, whether these fluctuations last for a long enough time to cause significant protein segregation. Composition fluctuations could be coupled to and stabilized by membrane shape fluctuations (24). Remarkably, heterogeneous model systems without any visible phase separation (i.e. above the miscibility critical temperature) were reported to show inhomogeneity on a length scale of tens of nanometers (25). The experiments discussed above are a few examples for recent work that has

led to doubts about the original "lipid raft" concept and to a more nuanced definition of "membrane rafts": "Membrane rafts are small (10 - 200nm), heterogeneous, highly dynamic, sterol- and sphingolipid-enriched domains that compartmentalize cellular processes. Small rafts can sometimes be stabilized to form larger platforms through protein-protein and protein-lipid interactions." (26).

If lipid composition is not driving membrane heterogeneity, could proteins be responsible for the formation of domains? The fact that the membrane is highly crowded (27) implies that protein-protein interaction play a dominant role. Indeed it was shown that proteins can form microdomains without involvement of lipid rafts (28). Historically, clathrin coated pits - membrane dimples caused by a cage of clathrin molecules - and caveolae - membrane invaginations formed by crosslinked caveolin molecules - were the first membrane micro domains to be identified. Moreover, the influence of proteins is not restricted to membrane proteins, the underlying cytoskeleton is believed to interact with the membrane, as well (29–34). A passive, flexible cytoskeletal network can cause membrane domains by exerting a force and deforming the membrane locally (33). In this model diffusion is influenced by steric repulsion between the network filaments and molecules in the membrane. A dynamic actin network has been shown to actively drive phase separation by the coupling of polymerization to membrane proteins that have spontaneous curvature (31, 32). In a different model, the "picket fence", the cytoskeleton affects the membrane indirectly via anchored transmembrane proteins. Those "pickets" are supposed to transiently confine proteins and lipids to nanometer sized domains (35). This idea has been challenged, by recent state of the art single-molecule fluorescence experiments (36), which do not find any confinement on length scales reported previously.

It seems that membrane heterogeneity cannot be ascribed to either lipids or proteins alone. Only if interactions between lipids and proteins (and other membrane constituents) are considered, the picture will be complete. Examples for these interactions are numerous. Proteins might assemble a shell of lipids around them (37, 38) whose size is comparable to possible "rafts" caused by lipid-lipid interactions (20) (Chap. 2 of this thesis). Crosslinking of GM1, a ganglioside and supposed lipid raft component, can induce phase separation in model membranes (39). The same happens if an actin network - as a model of the cortical cytoskeleton - is polymerized on the membrane (40). Proteins and peptides also

influence the line tension between coexisting lipid phases by binding to the domain boundary(41). For all these mechanisms for protein-lipid interaction to work the membrane could be a flat sheet. In fact, the plasma membrane and, especially, the membranes of inner organelles are curved with radii of curvatures from a few nm to μm (42–44). Curvature has been shown to influence processes like endocytosis and protein coat assembly (45–48) and phase separation of lipids (49). Since a lipid bilayer is elastic and resists bending (2) the question is, how membrane curvature is realized. As with the creation of heterogeneity, both lipids and proteins are involved (50). Membrane curvature affects lipid packing (51) and lateral lipid distribution (52). Also proteins interact via the curvature of the membrane (53–55), which can lead to sorting and thereby promotes heterogeneity (52, 56) (Chap. 4 of this thesis). Effects related to membrane curvature sensibly depend on material properties of the membrane, like bending rigidity and spontaneous curvature, which are functions of the lipid composition (22, 57) and depend on the properties of the extracellular matrix (58). Curvature is therefore another intermediary for the interplay of proteins and lipids: proteins modulate membrane curvature, lipids redistribute to regions with high or low curvature, changing the local composition, which influences curvature mediated effects and the curvature itself.

As the examples given above illustrate, there are many mechanisms by which membrane heterogeneity can be created. In a living cell all these processes take place at the same time and influence each other. Model membranes, however, allow one to study single processes separately in a controlled environment.

1.2 Artificial membranes

The influence of lipid composition on physical and chemical properties of the membrane can best be studied in a model system which allows complete control over the membrane's composition. To that end, giant unilamellar vesicles (GUVs) have proven to be one of the most versatile model membrane system. These closed, spherical single lipid bilayers of 10-100 μm diameter can be produced from a broad range of lipid compositions in physiologically relevant buffer conditions (59). They are free-standing and can be produced in sizes that are comparable to cells. While macroscopic (micrometer sized) lipid domains are absent in living cells, they can be

readily reconstituted and studied in GUVs (60). Alternatively, membrane domains are studied in supported lipid bilayers. However, it was found that interaction with the support influences the thermodynamic behavior of domains (61). In contrast to domains in GUVs, which are mobile and frequently fuse, the domains reconstituted in supported bilayers are practically static. The observed long term stability of domains corresponds therefore to a non-equilibrium situation. For these reasons we will restrict our discussion in the following to free-standing GUVs.

1.2.1 Formation and observation

Electroformation of GUVs Most commonly, GUVs are made by electroformation (62), a technique that provides a high yield of unilamellar vesicles of controllable lipid composition and size. Briefly, lipids are dissolved in an organic solvent and dried on the plates of a capacitor. The space between the plates is filled with an aqueous buffer and an oscillating electric field is applied. On the time scale of hours the electric field causes vesicles to swell from the lipid film and continue to grow by fusion. With electroformation it is possible to produce vesicles that consist of a mixture of phospholipids, cholesterol and sphingolipids, mimicking the composition of a cell membrane (60). In contrast to the cell membrane, however, there is no difference in composition between the leaflets in an electroformed vesicle. Also, in cells lipids are often attached to a carbohydrate (glycolipids), which is not the case in artificial membranes.

Below a certain critical temperature heterogeneous membranes spontaneously phase separate into two fluid phases, which requires the electroformation to be performed at a temperature above this critical temperature. Electroformation in its original form, pioneered by Angelova et al. (62) was not compatible with buffers of physiological salt conditions. This drawback can be overcome by the use of charged lipids (63), the exchange of the buffer in a flow chamber (64), or by using electric fields oscillating with much higher frequencies than in the original method (65). The approach devised by Montes et al. (65) permits the formation of GUVs from native membranes while preserving the compositional asymmetry between the leaflets, which is an important characteristic of biological membranes.

Microscopy on GUVs Due to their big size, GUVs are ideal for observation with standard microscopy techniques like phase contrast (59). From the vesicles' average shape (66) and the magnitude of thermal shape

fluctuations (67) important membrane material parameters, like bending rigidity and surface tension, can be obtained. The change of these material parameters can be followed through phase transitions (68) and their dependence on membrane composition can be studied (57). The use of artificial membranes for elucidating lipid driven heterogeneity was spurred by the work of Dietrich et al. (60, 69). They devised a method to directly visualize different liquid phases in phase separated GUVs, exploiting the differential partitioning of fluorescent probes. This method allowed the study of phase diagrams of phase separated membranes (3), see Fig. 1.3, and membrane material properties (20, 70, 71) (Chap. 2 of this thesis). The lateral lipid distribution on a molecular scale, however, is still inaccessible to current experimental techniques and can only be studied *in silico* (72).

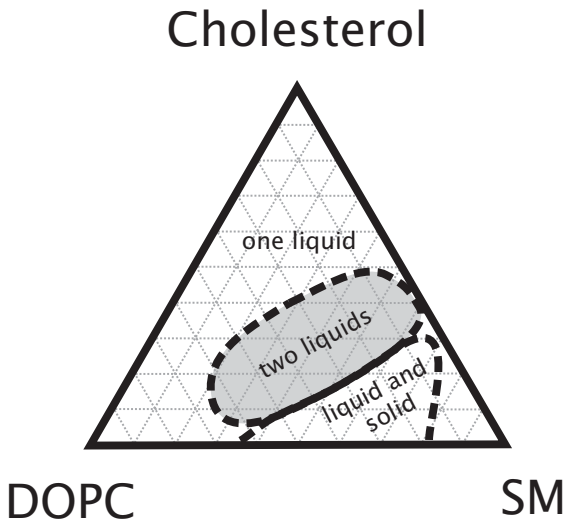

Figure 1.3
Phase diagram of a tricomponent vesicle consisting of phospholipids (DOPC), sphingolipids (sphingomyelin, SM) and cholesterol. Figure adopted from (73)

1.2.2 Selected results

Phase separation and material parameters Below a certain critical temperature, which depends on composition, heterogeneous vesicles phase separate (60). Such phase separated systems are most relevant to biology if the phases are both liquid. Tricomponent vesicles made from phospholipids, sphingolipids and cholesterol indeed exhibit a region of coexistence of two liquid phases, see Fig. 1.3, even at physiologically relevant tem-

peratures (73). After quenching the system from the homogeneous phase to the coexistence regime, the phase separation evolves by nucleation and domain coalescence or spinodal decomposition and coarsening (74).

While the two phases, named liquid ordered (L_o) and liquid disordered (L_d), are both characterized by a high lateral mobility of the lipids (75), they differ in the organization of the lipid tails, see Fig. 1.2. In the L_o phase, which is enriched in sphingolipids and cholesterol, the cholesterol intercalates between the sphingolipids and causes long range correlation between the lipid tails, hence this phase is called ordered. In the L_d phase which contains predominantly phospholipids, neighboring lipid tails interact only weakly and, due to the kink in the unsaturated acyl chains, there are more tail configurations possible. Because of the lack of orientational correlation between the tails this phase is called disordered.

The existence of two coexisting phases implies an energy connected to the interface between them. The interfacial energy per unit length is called line tension τ. Since the total energy of the interface is proportional to the length of the interface, the energy of a vesicle is decreased by coalescence of domains. The ground state should therefore be a completely phase separated vesicle, as shown in Fig. 1.4. Since the two phases differ in thickness (76), lipids at the interface have to bend or stretch, respectively, in order to avoid hydrophobic mismatch (77, 78), see Fig. 1.2. This mechanical energy contributes significantly to the line tension.

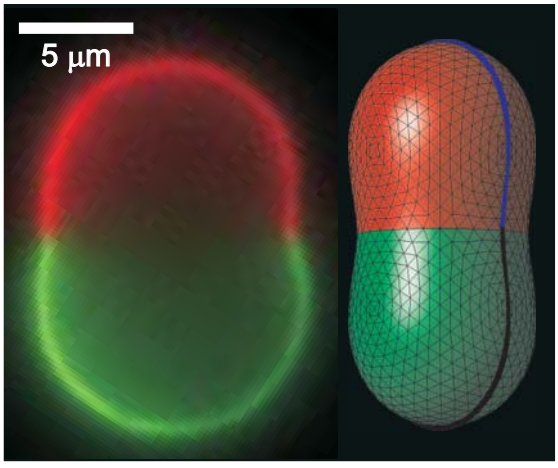

Figure 1.4
Left: Fluorescence microscopy image of a fully phase separated vesicle (equatorial section). The line tension manifests itself in the peanut shape (L_o phase shown in red, L_d phase shown in green); Right: Vesicle shape determined numerically from Eq. 1.1 with fitted analytical model for the contour (blue and black).

From a continuum point of view, the two phases can be characterized

by bulk material properties: surface tension σ, bending rigidity κ and Gaussian bending rigidity κ_{G}. For asymmetric membranes, the spontaneous curvature is another parameter to be considered; it gives the preferential curvature due to different composition of the two leaflets. The surface tension σ gives the energy needed to increase the membrane area with a fixed number of lipids. The concentration of free lipids in an aqueous buffer is negligibly low such that the number of lipids can be considered constant. In a relaxed vesicles (low-tension regime), the surface tension varies only weakly with vesicle surface area. This is due to the existence of thermal membrane fluctuations which are stretched out at increased tensions (79). In a tense vesicle the surface tension increases linearly with area, corresponding to an increased surface area per lipid. The shape of a vesicle also depends on the pressure difference between inside and outside, the Laplace pressure p.

While surface tension σ and pressure p are properties of individual vesicles, κ and κ_{G} only depend on membrane composition. Since the composition of the two phases changes with temperature, κ and κ_{G} effectively depend on temperature. The line tension strongly depends on the composition of the two phases -it vanishes at the critical point - and therefore on temperature as well (22), and it might also be influenced by lateral (surface) tension (80). The influence of all the material parameters are considered in the Canham-Helfrich energy (81, 82):

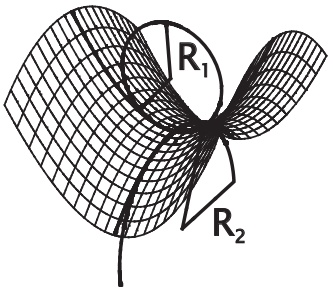

Figure 1.5
Principal radii

$$\mathcal{E} = \sum_{i=1,2} \int_{S_i} \left(2\kappa_i H^2 + \kappa_{\mathrm{G}}^{(i)} K + \sigma_i \right) \mathrm{d}A - pV + \tau \oint_{\partial S} \mathrm{d}\ell, \qquad (1.1)$$

The subscript i refers to the two phases, $H = 1/R_1 + 1/R_2$ the mean curvature and $G = 1/(R_1 R_2)$ the Gaussian curvature. R_1 and R_2 are the principle radii, see Fig. 1.5. Integration is over the surface of the phases S_i or the interface ∂S respectively. The shape of a vesicle can be found by minimization of this energy. As obvious from Fig. 1.4, the line tension is of prominent importance, leading to full phase separation and the characteristic 'peanut' shape.

Measurement of the thermal membrane fluctuations of the two phases allows the determination of the bending rigidities κ_i and surface tensions σ_i. For an infinite, two-dimensional, flat membrane in thermal equilibrium , the spectrum of out-of-plane fluctuations is

$$\left\langle |u_{\vec{q}}|^2 \right\rangle = \frac{1}{L^2} \frac{k_B T}{\sigma q^2 + \kappa q^4} \tag{1.2}$$

which follows from the Canham-Helfrich energy (82) and the equipartition theorem assuming periodic boundary conditions with period L. $u_{\vec{q}}$ is the Fourier component with wave vector $\vec{q}$. With the microscope we always observe a projection of the membrane which results in a one-dimensional contour, see Fig. 1.6, and a one-dimensional fluctuation spectrum. In phase separated vesicles we can use only the area around the vesicle poles for fluctuation analysis. The reason is that there, far away from the interface, the vesicle is very nearly spherical and the fluctuations can be measured relative to the mean radius (20) (Chap. 2 of this thesis). Using only a contour section of length a leads to a modification of the theoretically expected spectrum (83). Finally, the finite integration time for observation has to be taken into account, which influences the measured magnitude of long wavelength fluctuations, since those have a long correlation time (67). By consideration of all these effects the power spectral density of the shape fluctuations reads

$$\overline{\langle |u_k|^2 \rangle} = \underbrace{\sum_{q_x} \left(\frac{\sin((k-q_x)\frac{a}{2})}{(k-q_x)\frac{a}{2}} \right)^2}_{\text{finite contour section}} \times \tag{1.3}$$

$$\underbrace{\frac{L}{2\pi} \int_{-\infty}^{\infty} dq_y}_{\text{projection}} \quad \underbrace{\frac{k_B T}{L^2 2\eta q} \frac{\tau_q^3}{t^2} \left(\frac{t}{\tau_q} + \exp(-t/\tau_q) - 1 \right)}_{\text{spectrum averaged over acquisition time}}$$

with the length of the contour section a, $L = 2\pi R$, the vesicle radius R, absolute temperature T, viscosity of the surrounding medium η, camera integration/acquisition time t, $q = \sqrt{q_x^2 + q_y^2}$ and correlation time $\tau_q = (4\eta q)/(\sigma q^2 + \kappa q^4)$. Since this formula is derived for a flat membrane, it will deviate from the fluctuation spectrum of a closed, spherical vesicle, but only for the very lowest modes, which are long enough to feel the curvature of the vesicle (67). Fitting this expression to experimentally

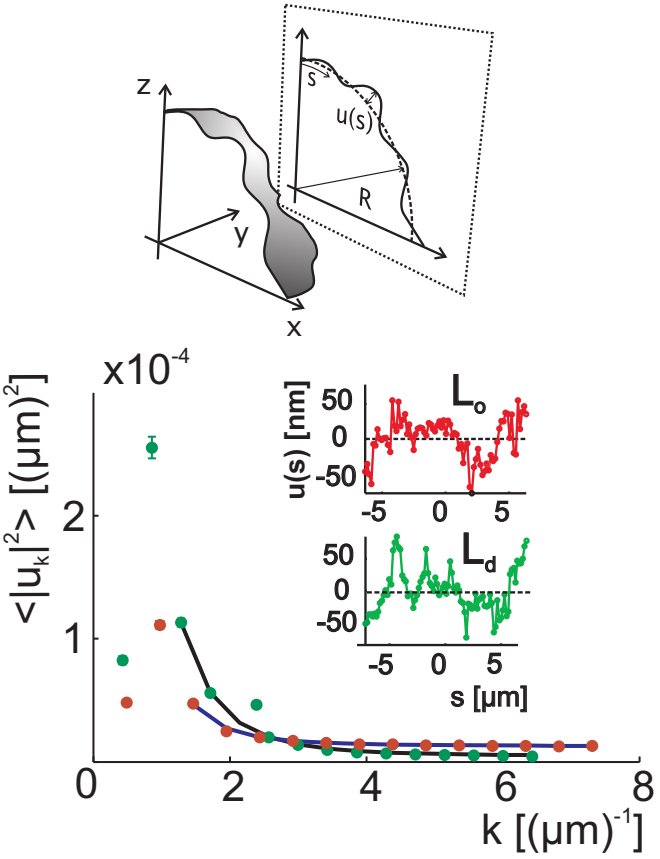

Figure 1.6
Top: The vesicle is projected along the y-axis on the plane of the camera (x-z plane). Fluctuations of the contour $u(s)$ are measured relative to the mean radius R of the approximately spherical vesicle poles. s is the arclength along the mean contour. Down: Typical experimental fluctuation spectra for the L_o phase (red dots) and the L_d phase (green dots) with fits of the theoretical expression for the spectrum, Eq. 1.3 (solid lines). Inset: Typical contour fluctuations.

determined fluctuation spectra for the two different phases reveals that the L_o phase is stiffer than the L_d phase (20) (Chap. 2 of this thesis), see Fig. 1.6. By detailed analysis of vesicle shapes, all membrane parameters can be determined (20, 71) (Chap. 2 of this thesis) including line tension and the difference in Gaussian bending moduli between the two phases. Alternatively, domain boundary fluctuations can be used to retrieve the

line tension (22, 84). Consistently, line tension around $1pN$ are found far away from the critical point where domain boundary fluctuations are absent. Close to the critical point, where domain boundaries fluctuate visibly, τ drops to $\approx 0.1pN$ and vanishes at the critical point. These values for the line tension suggest that small domains are stable against budding (85) and, taking into consideration active membrane recycling (86), domains in living cells should be at most $\approx 10nm$ in diameter (20) (Chap. 2 of this thesis).

Membrane mediated interactions Although complete phase separation is the ground state of a heterogeneous vesicle, domains with long term stability have been observed experimentally (70, 74, 87–89) (Chap. 3 of this thesis). Domain coalescence is kinetically hindered (88) which suggests an interaction between domains. As trapped coarsening is only observed in vesicles with budded domains, see Fig. 1.7, membrane mediated interactions (53–55) must be responsible for the observed effect.

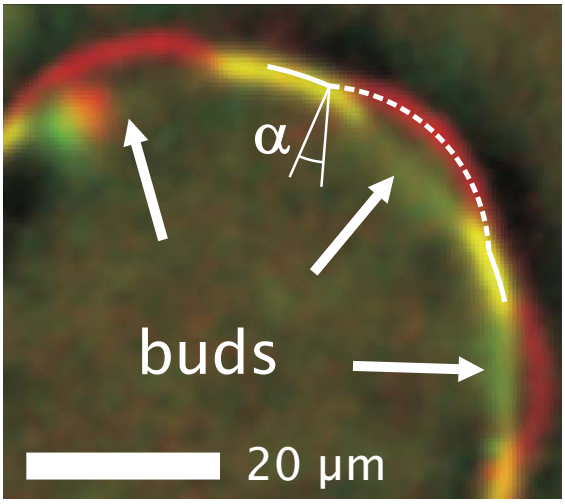

Figure 1.7
L_o buds (red) in a L_d background (yellow/green). α denotes the contact angle between the bud and the surrounding membrane.

This type of interactions is not restricted to membrane domains but also plays an important role for the organization of proteins (42, 53). Vesicles with bulged domains offers the unique possibility to study membrane mediated interactions exclusively, which would not be possible with proteins, due to their small size.

If the inter-domain forces are treated as harmonic springs, the spring

constant turns out to be $\approx 1 k_B T/\mu m^2$ (89) (Chap. 3 of this thesis), see Fig. 1.8.

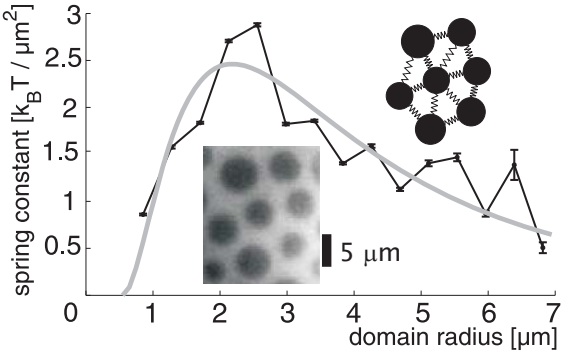

Figure 1.8
Spring constant k with respect to domain radius d (solid circles). The gray solid line shows a fit of Eq. 1.5 to the data. Left inset: L_o domains (dark) in an L_d background (bright). Right inset: Hookean spring model for domain interactions.

This value explains the long term stability of bulged domains (88) and their long range order. Membrane mediated interactions strongly depend on the strength of the distortions which are imposed by the inclusions (54) . Consequently, the spring constant varies with domain size: while it first increases with domain radius, reflecting increased distortion of the environment, it decreases for larger radii due to an increased distance to neighboring domains (89) (Chap. 3 of this thesis). Below a certain critical size ($< 0.5\mu m$), the force vanishes. This critical size is set by the invagination length $\xi = \kappa/\tau$ which gives the length scale where interfacial and bending energy are of the same magnitude (90, 91). In domains that are small compared to ξ the line tension cannot push out the domain against the bending rigidity and the domain stays 'flat'. In this shape it does not distort its environment and causes no interactions. Due to this effect, domains grow by coalescence until they reach the critical size. Domain fusion then becomes kinetically hindered which results in a preferred domain size (89) (Chap. 3 of this thesis), which grows only slowly (88).

To describe the system quantitatively, bulged L_o domains can be treated, to first approximation, as spherical inclusions which locally distort the surrounding membrane (54) and thereby cause and experience membrane mediated interactions (89) (Chap. 3 of this thesis). Since the L_o domains are much stiffer than the surrounding membrane in the L_d phase ($\frac{\kappa_o}{\kappa_d} \approx 4$ (20), Chap. 2 of this thesis) , it is a good approximation to consider them rigid. The interaction potential between two rigid inclusions in an infinite, asymptotically flat membrane was calculated in

(54):

$$V = 4\pi\kappa_{\mathrm{d}}(\alpha_1^2 + \alpha_2^2)\left(\frac{a}{r}\right)^4 \tag{1.4}$$

where r is the distance between the two inclusions, a is a cutoff length scale (typically the membrane thickness, $\approx$ 4nm), α_1 and α_2 are the domains' contact angles with the surrounding membrane (see Fig. 1.7) and κ_{d} is the bending modulus of the surrounding L_{d} phase. This result should approximately hold also for domains on a spherical vesicle if the domain radius is small compared to the radius of the vesicle. In general a domain is surrounded by many others. Therefore it is reasonable to assume that the domain moves in a harmonic potential with spring constant k. If the contact angle α and average domain distance grow linearly with domain size d, the dependence of k on d is given by:

$$k(d) = A\frac{(d - d_0)^2}{(r_0 + cd)^6}. \tag{1.5}$$

where r_0 and c are parameters which can be determined directly from the raw data and A and d_0 are fit parameters. Fig. 1.8 shows a fit of this expression to experimental data. The point d_0, where the interaction vanishes, is found to be close to the invagination length ξ (89) (Chap. 3 of this thesis).

Membrane mediated interactions are not necessarily repulsive. In coarse grained simulations, membrane mediated interactions induced the aggregation of small rigid caps (53). This suggests that the magnitude (and sign) of membrane mediated interactions depend on the length scale and membrane material properties.

Interestingly, it was found that membrane mediated interactions sort domains by size (56) (Chap. 4 of this thesis), see Fig. 1.9 Since big domains repel more strongly than small domains the total energy can be lowered by increasing the vesicle area covered by big domains. This can be achieved only if domains are sorted by size (56) (Chap. 4 of this thesis). Translated to proteins this might provide a mechanism for creating cell polarity or organize proteins on a large scale.

1.3 Living cells

The properties of a complex system can only be determined by examining the system itself: membrane heterogeneity must be studied ulti-

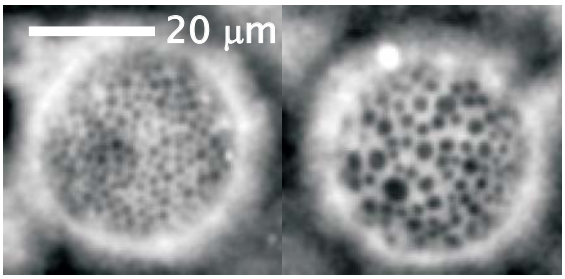

Figure 1.9
Two sides of the same phase separated vesicle. The L_d phase is fluorescently stained. The (dark) L_o domains in the two different regions show a marked difference in size.

mately in living cells. Processes during cell death, methods of cell fixation or preparation of cell extracts all potentially induce formation of domains. Since heterogeneities exist both on small length and time scales, advanced experimental methods capable of resolving theses scales must be employed. With FRET (Fluorescence Resonance Energy Transfer), for instance, spatial proximity between molecules in the nanometer regime can be measured (92), even at a single-molecule level (93). This technique is, however, limited to very small distances (typically $< 10nm$). Recently developed superresolution techniques (94) also deliver the necessary spatial resolution but suffer from a low acquisition speed. Up to now only techniques based on single molecule fluorescence or single particle tracking can address relevant length and time scales (95).

Single molecule techniques (96) have become a major tool for biophysics (97) and, lately, systems biology (98–100). The reason for that is twofold: first, single-molecule events can have biological relevance themselves (101) and second, the behavior of single molecules is a very sensitive readout for the characteristics of big ensembles. For instance, FRAP (Fluorescence recovery after photobleaching) is a well established technique to determine diffusion coefficients (102). However, FRAP averages over many molecules, which makes extensive modeling necessary to interpret the results (103). Here we discuss how signatures of membrane micro structure can be identified in single molecule tracking experiments.

1.3.1 Single molecule tracking

Single molecule tracking is based on the detection of the scattered or fluorescence light coming from a single particle or molecule that is coupled

to the molecule of interest. A successful experiments depends on the following key points: 1. A suitable probe has to be chosen that is both minimally perturbing and gives a sufficient signal. 2. The optical detection scheme has to be sensitive enough to detect the single probe and deliver the desired time resolution. Besides, photo destruction of the cell must be minimized. 3. The positions of the probe have to be determined with high, sub-diffraction resolution. 4. The kinetic parameters must be extracted from the molecule positions by constructing trajectories or analyzing directly spatio-temporal correlations. Besides the positions, the intensities of diffraction limited spots can be used to measure molecule numbers in these spots.

Probes Useful probes differ greatly in size, biocompatibiliy and photophysical properties. Gold particles provide an excellent signal to noise ratio and unlimited observation time, since their detection is based on light scattering. Gold is nontoxic and well-known surface chemistry allows them to be coupled to a wide range of molecules. The labeling ratio is, however, rather undefined and unspecific binding is an issue (36). Fluorescent quantum dots are considerably smaller than gold beads and possess good photostability (104, 105) though blinking might be a problem for some applications. The emission wavelength of quantum dots changes with their size which results in a broad spectrum of available colors. Quantum dots have to be coated to render them biocompatible and a one-to-one labeling ratio is difficult to achieve. Artificial dye molecules, like Cy5, are small but suffer from photobleaching. They can be coupled to molecules of interest by covalent bonds which guarantees monomeric labeling. For the study of proteins in living cells autofluorescent proteins are a good compromise between the probes discussed so far. They are intrinsically biocompatible and one-to-one labeling is easily achieved by fusing them to the protein of interest, which allows quantitative assessment of protein stoichiometry (106–108) (Chap. 7 of this thesis). Fluorescent proteins exist in different colors, which enables multiplexing. In contrast to all other probes also intracellular structures can be stained in a minimally invasive way. The biggest disadvantage of fluorescent proteins is their complex photophysics(109), especially the poor photostability (110). However, as we discuss below, improved data analysis techniques and optimization of experimental parameters can alleviate many of the problems related to photophysics (108, 111) (Chaps. 5 and 7 of this thesis). Recently, pho-

toactivatable fluorophores have been used to increase the number of signals which can be collected on a single cell (112).

Optical detection scheme Single molecules are usually detected with a microscope in widefield (113–116) or total internal reflection (117, 118) configuration. More elaborate ways of illumination have been developed to diminish background and minimize photodestruction (119, 120). A CCD camera is most commonly chosen as detection device. Their advantages comprise a high quantum yield, low noise and ability to image the whole field of view at once. A fluorescence signal coming from a single-molecule is described completely by the following parameters: intensity, spatial extension and polarization (or anisotropy), emission spectrum and, most importantly, position. All of these parameters contain relevant information about the molecule of interest and its local environment. As we discuss below, fluorescence intensity can be used to determine the stoichiometry of a molecule complex or assess membrane heterogeneity (108, 121) (Chap. 7 of this thesis). Anisotropy contains information about rotational diffusion of the probe (122, 123) and structural information (124). A shift of the emission spectrum reports changes in the local environment, e.g. the packing of lipids, if the used fluorescent probe is sensitive to those (125). Most importantly, the position of a fluorescent probe can be determined with a very high positional accuracy, down to a few nm (95). With the help of several focal planes (126) or by introducing an astigmatism (127), molecules can be localized in 3D.

Position determination Among the several methods to determine a molecule's position in 2D, fitting to the point spread function of the microscope is the most reliable procedure (128), see Fig. 1.10. The achievable positional accuracy depends on the signal to noise ratio (129, 130) and is typically 20-40 nm for fluorescent proteins in living cells (131). In fixed cells or with sufficient data acquisition speed, the single molecule positions can be combined to a high resolution image of the cell (94), a direct readout of heterogeneity. However, the lack of high temporal resolution conceals transient processes. Those processes manifest themselves in anomalous diffusion of single molecules addressed by single-molecule or single-particle tracking experiments (35, 36, 131–133). The achievable temporal resolution is typically a few ms for experiments in living cells (36, 131).

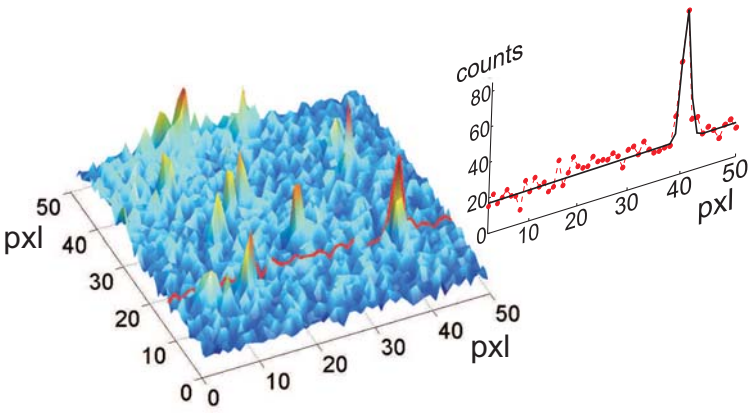

Figure 1.10
Left: Fluorescence signals coming from single molecules obtained in a live cell, right: 1D example for peak fitting. A gaussian (black) is fitted to the raw data (red) to determine intensity and position. pxl = 220 nm

Determination of kinetic parameters, PICS The recorded molecule positions are typically connected to trajectories (134–136) from which kinetic parameters are retrieved. The reconstruction of trajectories is, however, difficult, if the used fluorophore suffers from excessive blinking. Additionally, if the photostability is low, trajectories are short, which results in a big error in the calculated diffusion coefficients (137). Alternatively, kinetic parameters can be retrieved directly from spatio-temporal correlations of single molecule positions by Particle Image Correlation Spectroscopy (PICS) (111) (Chap. 5 of this thesis). This method is based on image correlation techniques (138) but exploits the high temporal and spatial resolution of single molecule tracking. In contrast to conventional tracking algorithms no *a priori* knowledge about diffusion speeds is required. PICS works for high molecule densities which makes it the ideal analysis method for experiments with photoactivatable fluorophores (112). Blinking and bleaching do not bias this method since uninterrupted trajectories are not required to determine mean squared displacements (MSDs) and eventually diffusion coefficients in a robust way. On the contrary, long lived dark states or reversible bleached states actually extend the accessible observation period compared to conventional tracking methods. In PICS a simple algorithm is used to determine the cumulative distribution

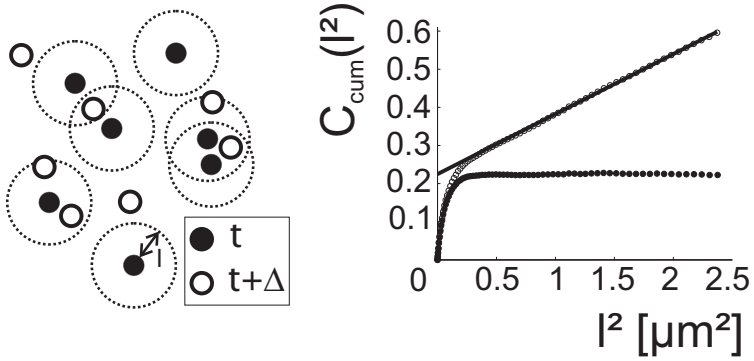

Figure 1.11
Left: PICS algorithm: count all molecules at time t_2 (open circles) which are closer than l (dashed circle) to a molecule at time t_1 (solid circles). Averaged over space and time this results in the cumulative correlation function $C_{\mathrm{cum}}(l, \Delta t)$ shown on the right (open circles). Subtraction of random correlations (solid line) results in the cumulative probability $P_{\mathrm{cum}}(l, \Delta t)$ apart from a normalization factor (solid circles).

function $P(l, \Delta t)$ for the length l of diffusion steps during the time lag Δt.

As shown in Fig. 1.11, the amount of molecules at time $t+\Delta t$ is counted that is closer than l to another molecule at time t. By subtraction of the linear contribution at bigger l - which stems from accidental proximity of uncorrelated molecules - $P_{\mathrm{cum}}(l, \Delta t)$ is obtained. If the diffusion coefficient D is determined directly from $P_{\mathrm{cum}}(l, \Delta t)$, assuming normal diffusion, the relative error is

$$\frac{\Delta D}{D} = \frac{1}{\ln 2}\sqrt{\eta^2 + (1 - (1/2)^{2/N})} \tag{1.6}$$

where N is the number of diffusion steps (= number of molecules per image $\langle m \rangle$ × number of image pairs M) and

$$\eta = \sqrt{16\pi \ln 2 \frac{cD\Delta t}{M}} \tag{1.7}$$

with the concentration of molecules c, diffusion coefficient D, time lag Δt and recorded image pairs M. While the first term under the root in Eq. 1.6 (η^2) is caused by the method, the second term is unavoidable and due to the stochastic nature of diffusion. Interestingly, the scaling behavior of η shows that the molecules can in principle be very dense and diffuse very

quickly on the time scale of a time lag Δt. If enough image pairs M are recorded, the error due to the method will be small.

To extract the MSD with respect to time lag Δt a model for the cumulative distribution function $P_{\text{cum}}(l, \Delta t)$ has to be fitted. For a homogeneous population of molecules diffusing normally the expected cumulative distribution function is (139)

$$P_{\text{cum}}(l, \Delta t) = 1 - \exp\left(-\frac{l^2}{4D\Delta t}\right) \tag{1.8}$$

This functional form very often does not give a good fit to the experimental data, since the behavior of the observed molecules is in general very heterogeneous. A population of molecules which exhibits two different diffusion coefficients D_1 and D_2 is represented by the following distribution function (132)

$$P_{\text{cum}}(l, \Delta t) = \alpha\left(1 - \exp\left(-\frac{l^2}{4D_1\Delta t}\right)\right) \tag{1.9}$$

$$+ (1-\alpha)\left(1 - \exp\left(-\frac{l^2}{4D_2\Delta t}\right)\right) \tag{1.10}$$

where α is the fraction of the molecules diffusing with D_1. Naturally, this distribution fits better than the distribution for a single fraction . However, the biological nature of the two fractions has to be determined carefully from the biological context on a case by case basis.

$P(l, \Delta t)$ can also be compared to distribution functions created by Monte Carlo simulations (140). The disadvantage of PICS is the loss of individual trajectories but the diffusion parameters obtained by PICS in an unbiased way can be used as initial parameters for elaborate tracking algorithms (134).

Analysis of fluorescence intensities Arguably the second most important parameter of a fluorescence signal is its intensity. By measuring the intensity stemming from a diffraction limited spot, the number of fluorophores can be determined. In this way it is possible to determine stoichiometry in biochemical reactions, count protein subunits (106) or quantify protein clustering due to heterogeneity (108) (Chap. 7 of this thesis). In single molecule experiments intensity is used in two ways to determine fluorophore numbers: the number of bleaching steps in multistep photobleaching is counted (106) or histograms of fluorophore intensities

are evaluated (107, 108, 121, 141) (Chap. 7 of this thesis). The complex photophysics, especially blinking, of autofluorescent proteins render both approaches difficult. Fluorescence traces do not show clear bleaching steps and intensity distributions are very broad, which obscures differences between e.g. monomers and dimers. However, it was shown that, with the right choice of experimental parameters, intensity histograms can be used for robust assessment of single-molecule stoichiometries (107, 108) (Chap. 7 of this thesis). If a fluorophore is illuminated so long that it bleaches during the illumination time, semi-classical Mandel theory predicts for the intensity distribution $p(n)$ (108) (Chap. 7 of this thesis)

$$p(n) = \frac{1}{N}\left(1 + \frac{1}{N}\right)^{-(n+1)} \tag{1.11}$$

where N is the mean number of photons detected. This prediction is readily verified in experiments (108) (Chap. 7 of this thesis), see Fig. 1.12. The intensity distributions of multimers can be derived by convolution of

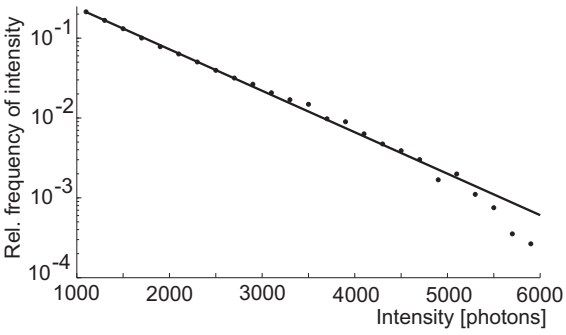

Figure 1.12
Logarithm of experimental intensity distribution of eYFP in living cells. The illumination time was 50 ms at an intensity of 3 kW/cm^2. A one-parameter fit of Eq. (1.11) (solid line) to the experimental intensity distribution for single YFPs (circles) gives $N = 837 \pm 3$ photons.

the monomer intensity distribution, Eq. 1.11, with itself (121).

Intensity histograms are also influenced by the thresholding procedure needed to separate signals from noise. Typically, the raw data is filtered to increase the signal to noise ratio. The matched filter principle (142) prescribes a filter that resembles the signal. For peaks with a width w, the raw images are therefore filtered with a Gaussian of width w. A peak in the filtered image is considered real if its intensity exceeds the noise level σ by a factor of t. The probability to detect a peak with width w and integrated intensity A at a noise level σ can be shown to be (108)

(Chap. 7 of this thesis)

$$p_{\mathrm{det}}(A;\sigma,w,t) = \frac{1}{2}\left(1 + \mathrm{erf}\left(\frac{A}{\sqrt{8\pi}\sigma w} - \frac{t}{\sqrt{2}}\right)\right) \tag{1.12}$$

Consequently, the measured intensity distributions are a product of the real intensity distribution of the molecule and Eq. 1.12. If the influence of the detection probability is properly taken into consideration, measured intensity distributions faithfully reflect underlying stoichiometry (108) (Chap. 7 of this thesis). To ensure that labeling stoichiometry is preserved, this method can be combined with the TOCCSL (Thinning out clusters while conserving stoichiometry of labeling) illumination scheme (143).

1.3.2 Selected results

GPCR signaling G protein coupled receptors, the biggest subfamily of membrane receptors, are a major drug target (144). Membrane heterogeneity is supposed to be involved in GPCR desensitization and internalization (13) and suspected to influence the kinetics of the signaling cascade (145). In the canonical model for GPCR signaling a ligand binds to the receptor on the outside of the cell, which, as a reaction, changes the conformation of its cytosolic part, see Fig. 1.13. This activation of the receptor enables it to interact with its G protein which may or may not be precoupled to the receptor. The G_α subunit of the G protein dissociates after interaction with the receptor and engages in downstream signaling. The activation of the G protein happens very quickly after ligand binding (146), which suggests that the receptor and its G protein are localized in micro domains or that they are coupled even in the absence of a ligand. Experiments addressing this precoupling give contradictory results (145, 147, 148). Application of Particle Image Correlation Spectroscopy to Adenosine A_1 receptor signaling revealed the influence of membrane heterogeneity and precoupling (11) (Chap. 6 of this thesis).

First of all, the dynamics of the Adenosine A_1 receptor is well described by a two-fraction model, Eq. 1.9. With the help of stimulation and decoupling experiments, the slow fraction was found to comprise receptors that interact with a G protein. Both the slow and the fast fraction show anomalous diffusion, see Fig. 1.14. This is evident from a non-linear dependence of the mean squared displacement on time. Normal diffusion,

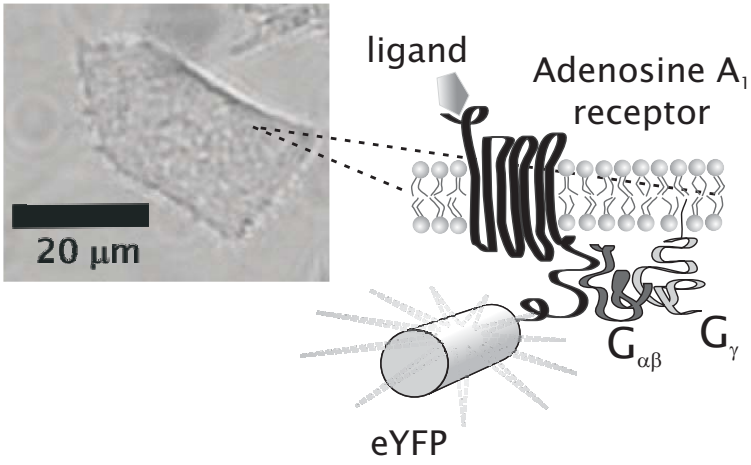

Figure 1.13
Left: Brightfield image of a living CHO cell transfected with the construct shown on the right. Right: G protein coupled receptor with its G protein which consists of three subunits α, β and γ. The receptor is tagged by eYFP fused to the C-terminus.

by contrast, is characterized by an MSD that increases linearly with time lag. In two dimensions the MSD is given by

$$\mathrm{MSD}_{\mathrm{normal}}(\Delta t) = 4D\Delta t \tag{1.13}$$

with a diffusion constant D.

Non-linear behavior can be introduced by membrane micro structure which interferes with the movement of the molecule. If the molecule is confined to a finite region of size L the MSD asymptotically becomes constant (29)

$$\mathrm{MSD}_{\mathrm{confined}}(\Delta t) = \frac{L^2}{3}\left[1 - \exp\left(-\frac{12D\Delta t}{L^2}\right)\right] \tag{1.14}$$

In the case of the Adenosine A_1 receptor, the slope of the MSD decreases for bigger time lags but stays finite. The receptor is not simply confined, its dynamics is better described by walking diffusion (133). In this model a molecule diffuses with diffusion coefficient D_{micro} within a domain of size L and the domain itself diffuses normally with diffusion coefficient D_{macro}, see Fig. 1.14. Consequently, the MSD of the molecule is the sum of the

MSD for normal and confined diffusion

$$\mathrm{MSD}_{\mathrm{walking}}(\Delta t) = \frac{L^2}{3}\left[1 - \exp\left(-\frac{12 D_{\mathrm{micro}}\Delta t}{L^2}\right)\right] + 4 D_{\mathrm{macro}}\Delta t \tag{1.15}$$

This functional form of the MSD can also arise in a different situation: In the hopping diffusion model a molecule is transiently confined to a domain with size L, diffusing with coefficient D_{micro}, see Fig. 1.14. Infrequently, the molecule hops to a neighboring domain which results in a smaller effective diffusion coefficient D_{macro} on length scales that are big compared to L. By fitting of Eq. 1.15 to experimental data for the Adenosine A_1 receptor D_{micro}, D_{macro} and L can be retrieved, see Fig. 1.14. Stimulation of the receptor with an agonist results in a decrease of the fast fraction. In other words, receptors translocate to microdomains with higher membrane viscosity upon ligand binding. These domains depend on the cytoskeleton, since they are not present in cell blebs. Probably, the cortical actin fosters the formation of membrane heterogeneities, like e.g. clathrin coated pits or caveolae. Additionally, it was shown that a fraction of the receptors is precoupled to the G protein: the fast fraction increases after decoupling of receptor and G protein. Probably, the G protein mediates the interaction with micro domains. In summary, micro domains as well as precoupling play crucial roles in Adenosine A_1 receptor signaling.

Clustering of H-Ras Another membrane protein which has been shown to translocate to microdomains upon activation is the small GTPase H-Ras (131). Ras proteins are involved in cell growth, proliferation and differentiation. The various isoforms, N-Ras, K-Ras and H-Ras activate several effectors to different extents. This specificity was speculated to depend on membrane domain localization since K-Ras and H-Ras mainly differ in their membrane-anchoring region. This notion was confirmed by electron microscopy studies (149), which showed that K-Ras and H-Ras membrane anchors are localized in distinct membrane domains that are tens of nanometers in size. FRET experiments show that Ras activation - i.e. binding of GTP- results in a decrease in mobility (93). A single particle study on constitutively active and inactive mutants of H-Ras showed, that a fraction of the active mutant is localized in micro domains (131). This confinement explains the decrease in mobility upon activation. Recently, this result was confirmed with the PICS method (111) (Chap. 5 of this

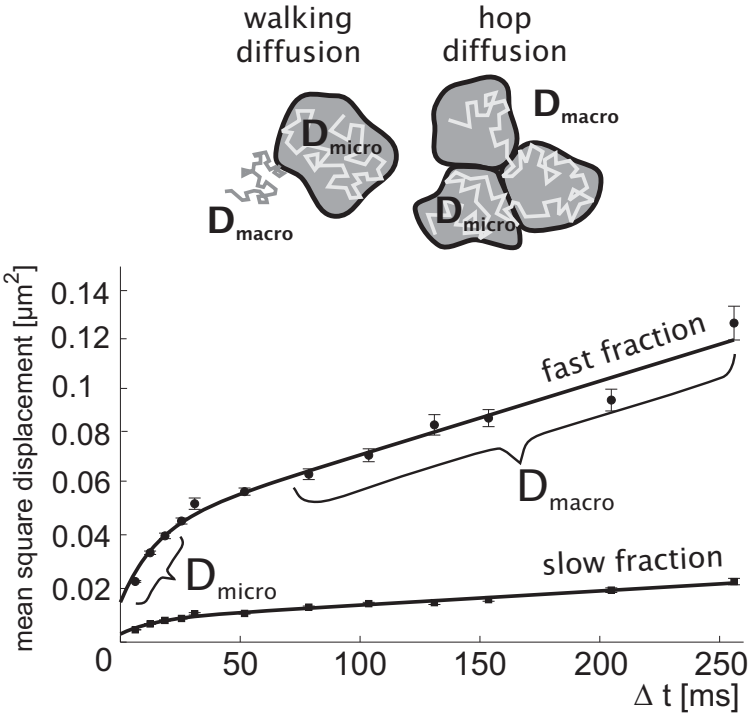

Figure 1.14
Mean square displacements of the Adenosine A_1 *receptors in living CHO cells. The fast receptor fraction is about 70 %. A fit to the walking diffusion model (solid line) yields for the fast fraction* $D_{micro} = 0.47 \pm 0.12 \mu m^2/s, D_{macro} = 0.07 \pm 0.01 \mu m^2/s, L = 287 \pm 20nm$ *and for the slow fraction* $D_{micro} = 0.10 \pm 0.02 \mu m^2/s, D_{macro} = 0.01 \pm 0.001 \mu m^2/s, L = 129 \pm 7nm$ *Inset: illustration for walking and hop diffusion. Both lead to an MSD with a bigger slope on small time scales (*D_{micro}*) and a smaller slope on long time scales (*D_{micro}*).*

thesis), see Fig. 1.15. Interestingly, the membrane anchor of H-Ras alone is found to localize in micro domains (150). Clustering of this membrane anchor was recently confirmed by a different method (108) (Chap. 7 of this thesis): analysis of the intensity histograms of YFP labeled anchors, as described above, revealed that they are found in clusters which cannot be explained by a random homogeneous distribution, see Fig. 1.16.

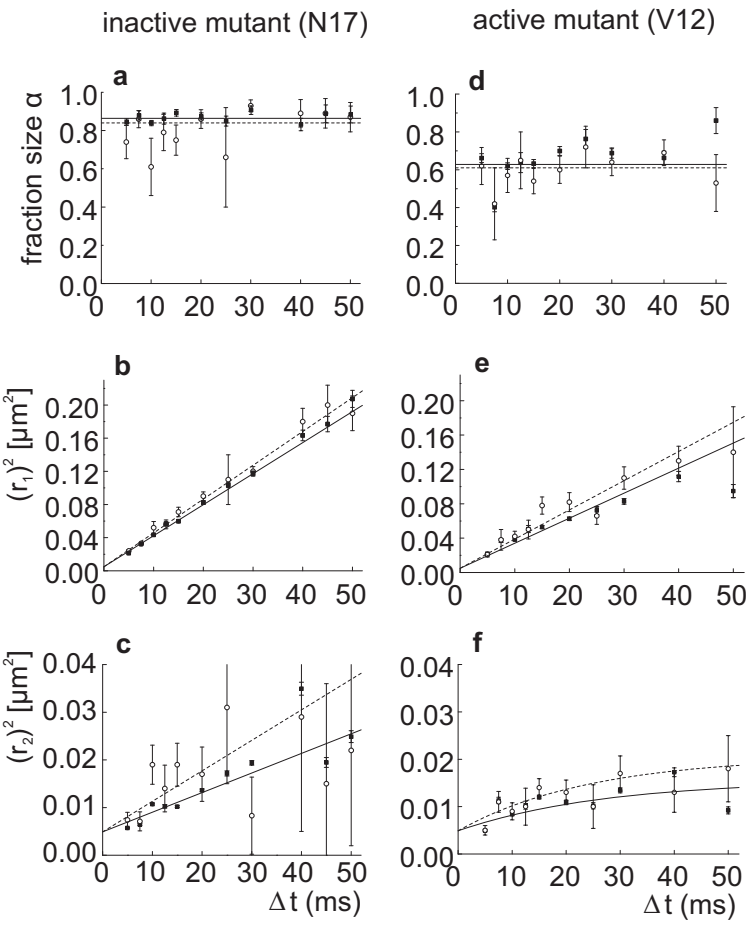

Figure 1.15
*Diffusional behavior of HRas. Fraction α (**a** & **d**) and mean square displacements r_1^2 (**b** & **e**) and r_2^2 (**c** & **f**) as functions of Δt for the constitutive inactive (N17) **(a-c)** and the constitutive active (V12) mutant (**d-f**) of HRas. The slow fraction of the active mutant **(f)** exhibits confined diffusion. Open circles / dashed lines correspond to conventional tracking results (131); solid squares / solid lines to results obtained by the PICS method. In the case of the conventional tracking errorbars correspond to the error of the fitting of the two fraction model, for PICS the size of the errorbars is given by Eq. 1.6.*

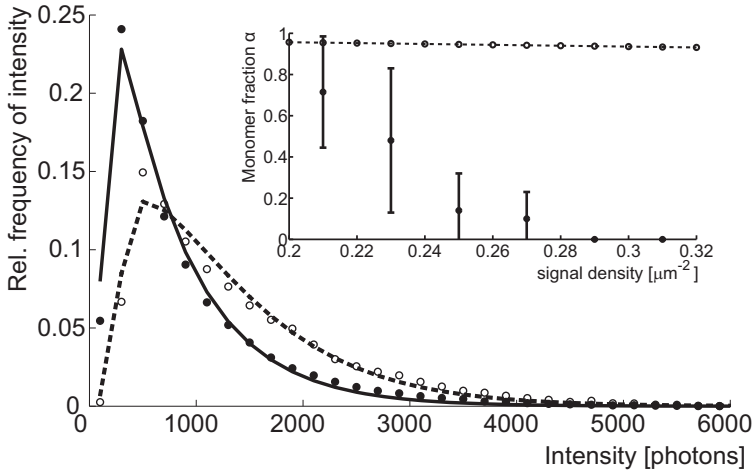

Figure 1.16
Intensity histograms of YFP labeled H-Ras membrane anchors. The solid circles correspond to a situation with only monomeric anchors (low molecule density). The open circles show the results for a higher peak density ($\rho = 0.25\mu m^{-2}$). The shift to higher intensities with increased density is due to the increased number of molecule dimers and higher multimers. The solid and dashed lines are fits to theoretical expressions for single-molecule intensity distributions. Inset: Fraction of monomers of the H-Ras membrane anchor in living CHO cells (circles). The solid line shows the theoretically expected monomer fraction for a uniform distribution of molecules.

1.4 Future directions

Experiments on living cells and artificial membranes have inspired and stimulated each other in the passed years and they will continue to do so. The challenge for the future is to bring both approaches closer together and the results to ever better and more quantitative agreement. Artificial membranes must be produced that resemble their living counterparts more closely while the necessary increase in complexity must not compromise the most important property of artificial systems: their controllability. Experiments on live cells, on the other hand, have to become more controlled and at the same time less invasive. Much progress can be made by developing ways to manipulate cells more specifically instead of using drugs that have many - sometimes unknown - effects. But improvements in both directions will be worthwhile since there are many open questions left.

If the membrane turns out to be indeed close to a miscibility phase transitions also *in vivo* the question is whether composition fluctuations are persistent enough to segregate proteins. Only then they could fulfill a significant biological function. To answer this it might be worthwhile to study the diffusion of peptides and proteins in GUVs (151, 152) that show strong composition fluctuations.

The nature of the coupling between the cytoskeleton and the membrane is still to be unraveled. Models range from indirect interactions via molecule pickets (30) to direct, mechanical coupling (31, 34). Only careful experiments in a clearly defined system can decide between these competing views. Those experiments start to be feasible due to recent progress on *in vitro* reconstitution of an actin cortex (153) and *in vitro* translation (154), both in GUVs. Models for the interaction between cytoskeleton and membrane predict asymmetric diffusion if the cytoskeleton is stretched (34). Stretching of the cell can be caused by a gradient in stiffness of the surrounding medium or simply during cell locomotion. The coupling of an asymmetric cell shape to non-isotropic diffusion might be important in processes like directional sensing and chemotaxis.

Concerning membrane mediated interactions, there are already quite a few *in vivo* experiments that showed a significant role of curvature in biological processes (45, 46) and more effects are predicted (155). The relation between membrane mechanics and biological processes, like signaling, is therefore likely to attract even more attention (156).

These questions and exciting technological developments conceived to answer them make membrane heterogeneity a lively field of research for years to come.